# Superconductivity and bosonic fluid emerging from moiré flat bands

Xu Zhang [1], Kai Sun,[2,*] Heqiu Li,[2,3] Gaopei Pan [4,5] and Zi Yang Meng [1,†]

[1]*Department of Physics and HKU-UCAS Joint Institute of Theoretical and Computational Physics,*
*The University of Hong Kong, Pokfulam Road, Hong Kong SAR, China*
[2]*Department of Physics, University of Michigan, Ann Arbor, Michigan 48109, USA*
[3]*Department of Physics, University of Toronto, Toronto, Ontario M5S 1A7, Canada*
[4]*Beijing National Laboratory for Condensed Matter Physics and Institute of Physics,*
*Chinese Academy of Sciences, Beijing 100190, China*
[5]*School of Physical Sciences, University of Chinese Academy of Sciences, Beijing 100190, China*

With the evidence of intervalley attraction-mediated by phonon or topological fluctuations, we assume the intervalley attraction and aim at identifying universal properties of moiré flat bands that shall emerge. We show that by matching the interaction strength of intervalley attraction with intravalley repulsion, the flat-band limit becomes exactly solvable. Away from the flat-band limit, the system can be simulated via quantum Monte Carlo (QMC) methods without sign problem for any fillings. Combining analytic solutions with large-scale numerical simulations, we show that upon increasing temperature, the superconducting phase melts into a bosonic fluid of Cooper pairs with large/diverging compressibility. In contrast to flat-band attractive Hubbard models, where similar effects arise only for on-site interactions, our study indicates this physics is a universal property of moiré flat bands, regardless of microscopic details such as the range of interactions and/or spin-orbit couplings. At higher temperature, the boson fluid phase gives its way to a pseudogap phase, where some Cooper pairs are torn apart by thermal fluctuations, resulting in fermion density of states inside the gap. Unlike the superconducting transition temperature, which is very sensitive to doping and twisting angles, the gap and the temperature scale of the boson fluid phase and the pseudogap phase are found to be nearly independent of doping level and/or flat-band bandwidth. The relevance of these phases with experimental discoveries in the flat-band quantum moiré materials is discussed.

## I. INTRODUCTION

As one of the most intriguing development in two-dimensional (2D) materials, moiré superlattices offer a new opportunity to access novel quantum states and quantum phenomena [1–4] such as flat bands at magic angle twisted bilayer graphene (TBG) or transition metal dichalcogenides (TMD) [5–7]. Recently, these systems were brought to the forefront of research by a series of intriguing experimental discoveries, such as correlated insulating states, continuous Mott transition, and superconductivity [8–34]. In addition to TBG, superconductivity has also been observed in other 2D materials such as $MoS_2$ [35,36], $NbSe_2$ [37], and possibly in twisted bilayer and double-bilayer $WSe_2$ [10,32], which is believed to be due to intervalley attractions [38–40]. In TBG, intervalley attractions were also considered as a key candidate mechanism for the superconducting state, though the origin of such attractions is still under investigation, i.e., whether it is phononic or has some more exotic (and even topological) mechanism [41–58].

Here, we focus on universal principles/properties that flat-band moiré superconductors shall obey/exhibit in that we introduce an intervalley attractive interaction and study its

nontrivial consequence. By matching intervalley attraction strength with intravalley repulsion, we find that at the flat-band limit, such systems can be solved exactly. Away from the flat-band limit, although an exact solution is absent, the model can be simulated via the momentum-space quantum Monte Carlo (QMC) method [59–61] without suffering the sign problem at any fillings, as the case in attractive Hubbard model [62–66]. By combining the exact analytic solution, exact diagonalization at small sizes, and the fully momentum-space QMC, we show that moiré flat-band superconductors exhibit a rich phase diagram, in sharp contrast to conventional Bardeen-Cooper-Schrieffer (BCS) superconductors. As shown in Figs. 2(a) and 2(b), at the temperature above the superconducting dome the system does not directly transform into a Fermi liquid. Instead, it first turns into a supercompressible bosonic fluid phase, where fermionic excitations are fully gapped but the compressibility is high and increases/diverges upon cooling. This physics is in strong analogy to the flat-band attractive Hubbard model [67,68], but also with clear differences. In the flat-band Hubbard model, the same type of physics only arises when the interactions are strictly on-site, and nononsite interactions, such as nearest neighbor, quickly lead to other physics, e.g., phase separation [68]. In contrast, for moiré flat bands, our studies indicate that the exact solution and related phenomena are extremely robust and fully insensitive to such microscopic details. No matter if the interaction

---

*sunkai@umich.edu
†zymeng@hku.hk
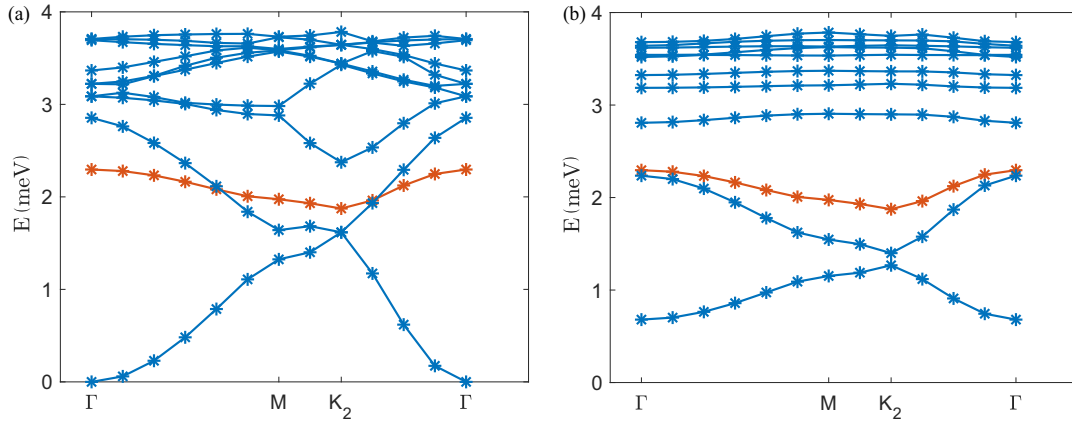
FIG. 1. Excitation spectrum for intervalley attractive and repulsive model where the system size is $12 \times 12$ and parameters come from Appendix A. (a) Single-paritcle excitation (red line) and Goldstone excitation (blue lines) along high symmetry line for intervalley attractive model. (b) Single-paritcle excitation (red line) and gapped charge neutral excitation (blue lines) along high symmetry line for intervalley repulsive model.

is short range or longe range and no matter if the spin-orbit coupling is weak (e.g., graphene) or strong (TMD), our exact solution and all qualitative features remain the same. This robustness is of crucial importance for the experimental study of moiré lattices where on-site interactions are not expected to be dominant and the spin-orbit effect may or may not be strong depending on the materials. As one further increases the temperature, this bosonic fluid gives way to a pseudogap phase where fermion states start to emerge inside the gap and gradually fill it up upon increasing the temperature. These nontrivial sequence of phase transitions/crossovers arise at filling range larger than the superconducting dome and sur-

vive to a temperature much higher than the superconducting transition $T_c$.

The bosonic fluid phase can be viewed as a liquid of Cooper pairs, where, although the Cooper pairs have fully formed, (quasi)-long-range phase coherence has not yet been developed due to strong fluctuations. Experimentally, the key signature of this phase is a large single-particle gap around the Fermi energy, combined with a high/diverging compressibility. The pseudogap phase is a partially melted boson liquid, where thermal fluctuations start to tear apart some of the Cooper pairs, feeding the single fermion spectral weight into the energy gap.
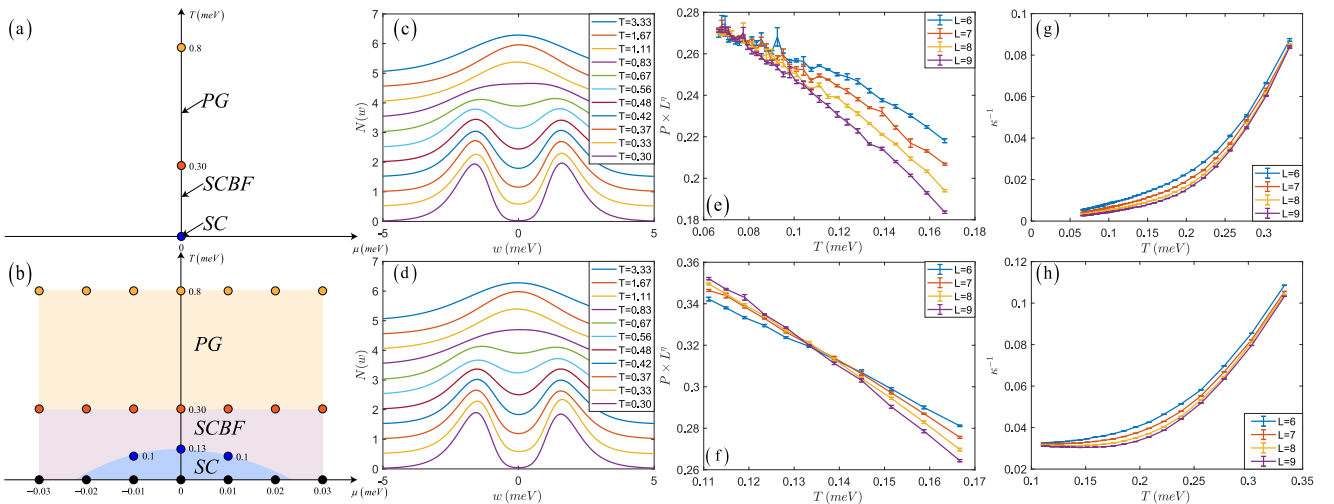


FIG. 2. QMC simulations of the flat-band limit (top row) and away from the flat-band limit (bottom row). The bandwidths of noninteracting band structures are set to 0 and 0.8 meV, respectively. (a,b) Phase diagrams. In the flat-band limit (a), a finite chemical potential drives the system into a trivial insulator with either empty ($\mu \ll 0$) or completely filled ($\mu \gg 0$) bands. In (b), the yellow/purple region is the pseudogap (PG)/supercompressible bosonic fluid (SCBF) phase, and the blue region marks the superconducting (SC) dome. (c,d) Density of states for a $9 \times 9$ system at $\mu = 0$. The Cooper gap survives above the superconducting transition temperature and turns into a pseudogap above $T \sim 0.3$. (e,f) Critical scaling of $P \times L^\eta$ versus $T$ with Berezinskii-Kosterlitz-Thouless (BKT) anomalous dimension $\eta = 1/4$. The crossing point of different system sizes ($L = 6, 7, 8, 9$) marks the superconducting transition temperature: $T_c \sim 0$ in (e) and $\sim 0.13$ in (f). (g,h) Inverse of compressibility $\kappa$ for $L = 6, 7, 8, 9$ at $\mu = 0$. At low temperature, diverged compressibility $\kappa$ in (g) converges in superconducting phase as shown in (h).

Simulations and analytic theory also indicate that the crossover temperatures between the normal fluid and the pseudogap phase (or between the pseudogap and the bosonic fluid phases) are dictated by the energy scale of the intervalley attractions, and is nearly independent of filling levels or flat-band bandwidth. In contrast, the superconducting transition temperature depends strongly on the bandwidth of the flat band, as well as filling fractions. In the QMC simulations, a superconducting dome is observed, which is qualitatively consistent with the experimental observations in TBG and TMD systems with the chemical potential partially filling all flat bands [10,13,15,32]. As the bandwidth reduces to zero (i.e., towards the flat-band limit), the height of the dome (i.e., the superconducting transition temperature) decreases to zero, although the noninteracting density of states (DOS) for the flat band diverges.

## II. MODEL

We consider a generic system with two valleys, labeled by the valley index $\tau$ and $-\tau$, respectively, connected by the time-reversal transformation $(T\tau = -\tau)$. In the flat-band limit, kinetic energy can be dropped once other bands are projected out. For interactions, we define it in the momentum space as

$$H_I = \frac{1}{2\Omega} \sum_{\mathbf{G}} \sum_{\mathbf{q}\in mBZ} V(\mathbf{q}+\mathbf{G})\delta\rho_{\mathbf{q}+\mathbf{G}}\delta\rho_{-\mathbf{q}-\mathbf{G}}, \qquad (1)$$

where $\mathbf{q}$ is the momentum transfer in a moiré Brillouin zone (mBZ) and $\mathbf{G}$ is the moiré reciprocal lattice vector. We set the interaction strength $V(\mathbf{q}+\mathbf{G})$ to be an arbitrary positive function and $\delta\rho_{\mathbf{q}+\mathbf{G}}$ is the density difference between two valleys

$$\delta\rho_{\mathbf{q}+\mathbf{G}} = \rho_{\tau;\mathbf{q}+\mathbf{G}} - \rho_{-\tau;\mathbf{q}+\mathbf{G}}, \qquad (2)$$

where $\rho_\tau$ and $\rho_{-\tau}$ are the fermion density from the two valleys. In the band basis, $\delta\rho$ can be projected to the flat band

$$\delta\rho_{\mathbf{q}+\mathbf{G}} = \sum_{\mathbf{k},m,n}[\lambda_{m,n,\tau}(\mathbf{k},\mathbf{k}+\mathbf{q}+\mathbf{G})c^\dagger_{\mathbf{k},m,\tau}c_{\mathbf{k}+\mathbf{q},n,\tau}$$
$$- \lambda_{m,n,-\tau}(\mathbf{k},\mathbf{k}+\mathbf{q}+\mathbf{G})c^\dagger_{\mathbf{k},m,-\tau}c_{\mathbf{k}+\mathbf{q},n,-\tau}], \quad (3)$$

where the form factor $\lambda$ is computed via the unitary transformation between the plane-wave basis and the band basis (see Appendix A for details). This interaction contains intervalley attraction and intravalley repulsion with the same strength $V$, and this is how intervalley attractions are introduced in our model. With this interaction, this model is exactly solvable in the flat-band limit, while away from the exactly solvable limit (i.e., with the finite bandwidth and chemical potential), it can be simulated via QMC without sign problem.

## III. EXACT SOLUTION

After dropping the trivial kinetic energy, the flat-band limit of our Hamiltonian is reduced to $H = H_I$ [Eq. (1)], which can be solved exactly due to an emergent SU(2) symmetry with generators

$$\sigma_x = \Delta + \Delta^\dagger, \sigma_y = i(\Delta - \Delta^\dagger), \quad \sigma_z = \hat{N}_p - N_d, \quad (4)$$

where $\Delta^\dagger = \sum_{\mathbf{k},m} c^\dagger_{\mathbf{k},m,\tau}c^\dagger_{-\mathbf{k},m,-\tau}$ and $\Delta = \sum_{\mathbf{k},m} c_{-\mathbf{k},m,-\tau}c_{\mathbf{k},m,\tau}$ creates/annihilates one intervalley Cooper pair and $\hat{N}_p$ is the particle number operator of flat bands. The constant $N_d$ is the max electron number that these flat bands can host in one valley. It is easy to verify that these three operators obey the $\mathfrak{su}(2)$ algebra $[\sigma_i, \sigma_j] = 2i\epsilon_{ijk}\sigma_k$ and they all commute with $\delta\rho$ and $H_I$, $[\sigma_i, H_I] = 0$. In other words, these three operators generate a SU(2) symmetry group.

This emergent SU(2) symmetry and exact solution are in analogy to the flat-band Hubbard model [67] and the SU(4) emergent symmetry of TBG flat bands [69–72], but there are some key differences. For the Hubbard model, the emergent symmetry and exact solution only arises when the interaction is on-site and the interactions beyond on-site (e.g., nearest neighbor) take away the exact solution and results in other instabilities like phase separation [68]. In contrast, our exact solution is insensitive to the range and/or the functional form of interactions. It is also worthwhile to highlight that the attractive Hubbard model can be exactly mapped to a repulsive Hubbard at half filling via a particle-hole transformation. Such a mapping does not exist in general for moiré flat bands because the particle-hole transformation will change the $\lambda$ function used in the flat-band project. For the inter-valley repulsive model at half filling

$$\delta\rho'_{\mathbf{q}+\mathbf{G}} = \rho_{\tau;\mathbf{q}+\mathbf{G}} + \rho_{-\tau;\mathbf{q}+\mathbf{G}}$$
$$= \sum_{\mathbf{k},m,n} \lambda_{m,n,\tau}(\mathbf{k},\mathbf{k}+\mathbf{q}+\mathbf{G})$$
$$\times (c^\dagger_{\mathbf{k},m,\tau}c_{\mathbf{k}+\mathbf{q},n,\tau} - \bar{c}^\dagger_{\mathbf{k},m,-\tau}\bar{c}_{\mathbf{k}+\mathbf{q},n,-\tau}). \quad (5)$$

Here, we use the particle-hole transformation $\bar{c}_{\mathbf{k},m,-\tau} = c^\dagger_{-\mathbf{k},m,-\tau}$. It is obvious that ground states for a general intervalley repulsive model have valley polarized $Z_2$, not SU(2) symmetry. This difference can also be seen in charge-neutral excitation spectrums as shown in Fig. 1. One can see that, although the two models share the same single-particle excitation spectrum as the red lines in Figs. 1(a) and 1(b), their two-particle spectra are totally distinct [i.e., continuous excitation in Fig. 1(a) and gapped in Fig. 1(b) as the blue lines indicate]. The attractive model is gapless due to the Goldstone mode from the SU(2) symmetry, while the repulsive one is gapped due to the absence of SU(2) symmetry and Goldstone modes. We will show how to derive exact solutions briefly below and leave the details for Appendix D.

Because our Hamiltonian is semi-positive-definite [$V > 0$ in Eq. (1)], two obvious zero-energy ground states can be immediately identified: The empty and fully filled states labeled by $|\psi_0\rangle$ and $|\psi_{2N_d}\rangle$, where $\delta\rho|\psi_0\rangle = \delta\rho|\psi_{2N_d}\rangle = 0$. In terms of the SU(2) symmetry group, these two states are fully polarized states of the $\sigma_z$ operator, known as the highest weight states, where the eigenvalues of $\sigma_z$ reach the highest/lowest possible values $\pm N_d$. Due to the SU(2) symmetry, any SU(2) rotation of these two ground states must also be a degenerate ground state. Here, we can use $\Delta^\dagger$ and $\Delta$ as raising and lowering operators of the $\mathfrak{su}(2)$ algebra, and generate all the degenerate ground states from the empty state $|0\rangle \equiv |\psi_0\rangle$

$$|\psi_{2n}\rangle \equiv \sqrt{\frac{(N_d-n)!}{n!(N_d)!}}(\Delta^\dagger)^n|0\rangle, \qquad (6)$$

where $0 \leqslant n \leqslant N_d$ and $|\psi_{2n}\rangle$ is the degenerate ground state with $2n$ fermions. Another way to understand these degenerate ground states is to realize $[H_I, \Delta^\dagger] = 0$ implies that it costs no energy to create a Cooper pair. Thus, we can introduce an arbitrary number of Cooper pairs to the empty state and obtain a degenerate ground state $|\psi_{2n}\rangle$ with $n$ Cooper pairs. It is worthwhile to highlight that the BCS wave function $\psi_{\text{BCS}} = \frac{1}{\mathcal{N}} \exp(\frac{v}{u} \Delta^\dagger)|0\rangle$ is also an exact ground state of this model. But this one is nothing unique and just one of $N_d + 1$ degenerate ground states. The BCS wave function may not be favored when the kinetic term and chemical potential are introduced since the chemical potential term will favor a certain filling but not mixing states with different particle number.

In the exact solution, the single-particle correlation function can be computed by noticing $c_{\mathbf{k},\tau}^\dagger|\psi_{2n}\rangle = \sqrt{\frac{N_d-n}{N_d}}|\psi_{2n+1,\mathbf{k},\tau}\rangle$, $c_{\mathbf{k},\tau}|\psi_{2n}\rangle = \sqrt{\frac{n}{N_d}}|\psi_{2n-1,-\mathbf{k},-\tau}\rangle$, where $|\psi_{2n+1,\mathbf{k},\tau}\rangle \equiv \sqrt{\frac{(N_d-n-1)!}{n!(N_d-1)!}}(\Delta^\dagger)^n c_{\mathbf{k},\tau}^\dagger|0\rangle$. As shown by the red line in Fig. 1, single-particle excitation is fully gapped and independent with intervalley interaction (no matter the repulsion or attraction). For repulsive interactions, the gap is an insulating gap without another charged excitation inside [70–74]. In our model, this gap is the Cooper gap, i.e., the energy cost to break a Cooper pair. The Cooper gap scales linearly with interaction energy $V$ and there are continuously charged excitations within the gap such as the blue line in Fig. 1(a). Thus, at low temperature $T \ll V$, all electrons are paired into Cooper pairs, i.e., the system is a fluid of Cooper pairs without unpaired fermions.

We can also compute the correlation function of Cooper pairs $\langle\Delta(t)\Delta^\dagger(0)\rangle$ by noticing $\Delta^\dagger|\psi_{2n}\rangle = \sqrt{(N_d-n)(n+1)}|\psi_{2n+2}\rangle$. Because $[H_I, \Delta] = [H_I, \Delta^\dagger] = 0$, this correlation function is time independent at any temperature. At $T = 0$, this correlation function is

$$\langle\Delta(t)\Delta^\dagger(0)\rangle = \frac{N_d(N_d+2)}{6} \sim \frac{N_d^2}{6}, \qquad (7)$$

which is in good agreement with QMC simulations [see Figs. 4(a) and 4(b)]. It is also worthwhile to point out that, in the thermodynamic limit, this $N_d^2$ scaling diverges faster than the system size, indicating an instability towards superconductivity at $T = 0$.

Despite the finite Cooper gap and diverging superconducting correlation function, Cooper pairs in this boson fluid do not lead to superconducting at any finite temperature. This is because the superconducting order parameter is part of a SU(2) generator. Therefore, a superconducting state would spontaneously break the SU(2) symmetry instead of just the U(1) charge symmetry. In other words, the symmetry breaking pattern here is in the Heisenberg universality class, instead of $XY$. For 2D systems at finite $T$, it has long been known that thermal fluctuations will destroy any order that spontaneously breaks a SU(2) symmetry (i.e., there is no finite temperature order for Heisenberg spins in two dimensions). Thus, although Cooper pairs have formed at $T \sim V$, long-range or quasi-long-range phase coherence cannot be developed at any finite temperature. This conclusion is verified in QMC simulations, where we observe a fully developed Cooper gap at finite $T$, but the phase coherence remains disordered even down
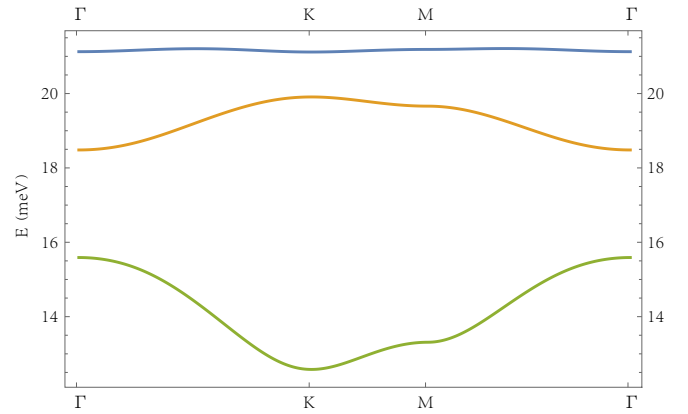


FIG. 3. Dispersion of the top three bands in mBZ.

to the lowest accessible temperature [Figs. 2(a), 2(c) 2(e), and 2(g)]. In addition to preventing the formation of a finite $T$ superconducting phase, the SU(2) symmetry also offers an interesting link between superconductivity fluctuations and particle-number fluctuations. From the SU(2) symmetry, we have $\langle\sigma_z^2\rangle = \langle\sigma_x^2\rangle$ and thus $\langle\hat{N}_p^2\rangle - \langle\hat{N}_p\rangle^2 = 2\langle\Delta\Delta^\dagger\rangle$. Because superconductivity fluctuations diverge as $\propto N_d^2$ at $T = 0$, particle-number fluctuations must also diverge as $\propto N_d^2$. This scaling violates one fundamental assumption of statistical physics, the central limit theorem, which requires square fluctuations to scale linearly with system sizes. Such a violation is a consequence of the infinite ground-state degeneracy.

From the fluctuation-dissipation theorem, this divergence in particle-number fluctuations implies a diverging compressibility at low $T$: $\kappa = \frac{1}{N_d}\frac{d\langle\hat{N}_p\rangle}{d\mu} = \beta\frac{\langle\hat{N}_p^2\rangle - \langle\hat{N}_p\rangle^2}{N_d} = \frac{2\beta}{N_d}\langle\Delta\Delta^\dagger\rangle$. When the temperature is reduced, $\kappa$ increases. In the low-temperature limit, because $\langle\Delta\Delta^\dagger\rangle \propto N_d^2$, $\kappa$ diverges as $\kappa \propto \beta N_d$. This divergence is also seen in the QMC simulations in Fig. 2(g).

In summary, in the flat-band limit, exact theory analysis predicts a bosonic fluid of Cooper pairs within a full Cooper gap. This bosonic fluid has a high compressibility, which diverges at $T \to 0$. To highlight this diverging compressibility, we call this state the supercompressible bosonic fluid (SCBF) in our phase diagrams in Figs. 2(a) and 2(b).

## IV. ED AND QMC SIMULATIONS

For simplicity, here we only consider one flat band per valley and choose parameters according to twisted homobilayer TMDs [75,76] to carry out exact diagonalization (ED) and QMC simulations (see Fig. 3 and Appendix A). The same techniques can also be applied to systems with more flat bands (e.g., TBGs), and all qualitative features shall remain. We first simulate systems with sizes $3 \times 3$ and $3 \times 4$ (number of momentum points in mBZ) via ED. The number of ground states and single-particle excitations perfectly match the analytic theory (see Fig. 5). The implementation of the momentum space QMC simulation are shown in Appendixed B and C, where we prove the absence of sign problem at any fillings and regardless of bandwidth. This allows us to efficiently simulate this model (for system size up to $9 \times 9$) and explore
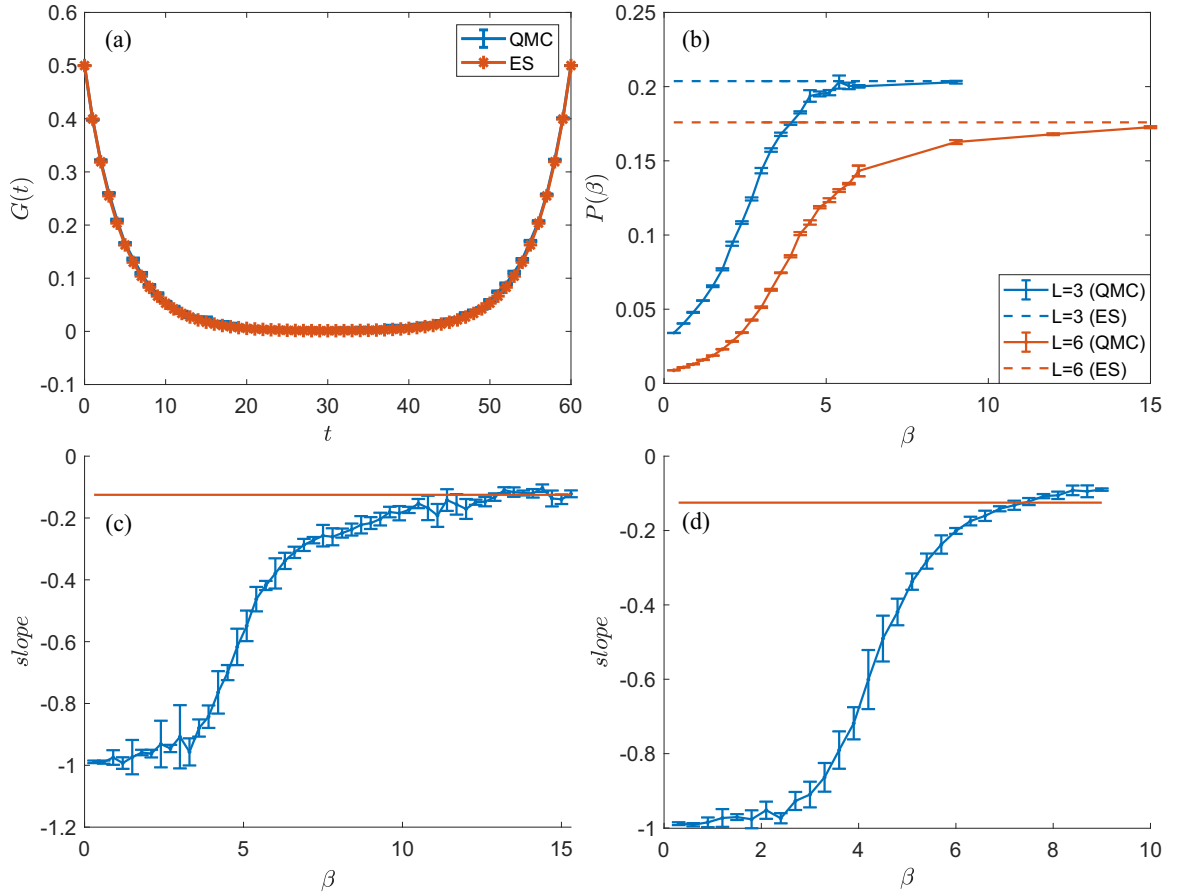
FIG. 4. Benchmark results for QMC. (a)–(c) are results at flat-band limit, (d) is simulated with kinetic term. (a) The blue line is the single-particle Green's function for $9 \times 9$ momentum mesh in mBZ with $\beta = 6$ at $\Gamma$ point from QMC, while the red line is the exact solution (ES) according to Eq. (D3). (b) Superconductivity pairing correlation function for $3 \times 3$ and $6 \times 6$ systems from QMC and ES. ES result comes from Eq. (D4). (c,d) slope $= \frac{d \ln(P)}{d \ln(L^2)}$ vs $\beta$ at $\mu = 0$. At the superconducting transition temperature, this slope shall reach $-\frac{\eta}{2} = -\frac{1}{8}$ (the red horizontal line), in good agreement with Figs. 2(e) and 2(f).

the phase space both at and away from the flat-band limit. For a benchmark, we compute the single-particle Green's function and superconductor correlation function at the flat-band limit,
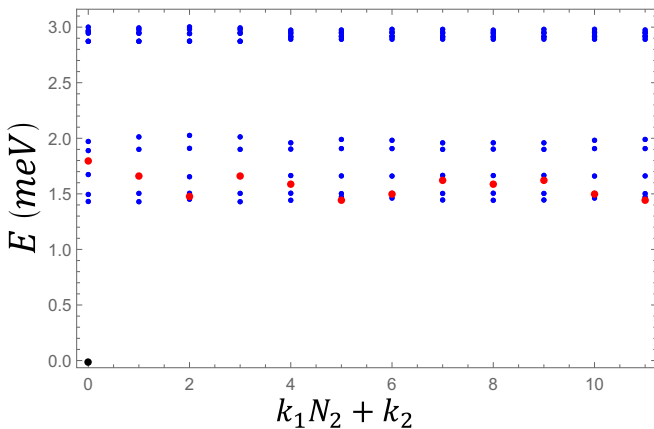


FIG. 5. ED results for $3 \times 4$ system at particle number $N = 12$ and $N = 11$. Black point represents ground state, red points are single-particle excitations, and blue points are all one-charge excitations.

which agree nicely with the analytic theory [see Figs. 4(a) and 4(b)].

With the imaginary-time correlation functions obtained in QMC, we further employ the stochastic analytic continuation (SAC) method to extract the real-frequency spectra [61,77–87]. In Figs. 2(c) and 2(d), we plot the fermion DOS at different temperature for a $9 \times 9$ system. At $T < 0.3$, a full gap is observed, which is the Cooper gap discussed above. For $0.3 < T < 0.8$, the fermion spectral weight starts to emerge inside the gap, i.e., a pseudogap (PG) is formed. Defining $P = \frac{1}{2N_d^2} \langle \Delta \Delta^\dagger + \Delta^\dagger \Delta \rangle$, we also try to determine the superconducting phase transition temperature $T_c$ by probing the onset of quasi-long-range order. This is achieved via the data cross of $P \times L^\eta$ versus $T$ as shown in Figs. 2(e) and 2(f) and by comparing the slope of $\frac{d \ln(P)}{d \ln(L^2)}$ versus $\beta$ [see Figs. 4(c) and 4(d)] with the BKT anomalous dimension exponent $\eta = \frac{1}{4}$ [66,88–90], using $P = L^{-\eta} f[L \cdot \exp(-\frac{A}{(T-T_c)^{1/2}})]$. In Fig. 2(e) for the case of the flat-band limit, the cross point is indeed approaching $T_c \to 0$, confirming the absence of a finite temperature phase transition, in full agreement with the exact solution.

With the exactly solvable limit understood, a kinetic energy term with finite (but small) bandwidth is introduced, which
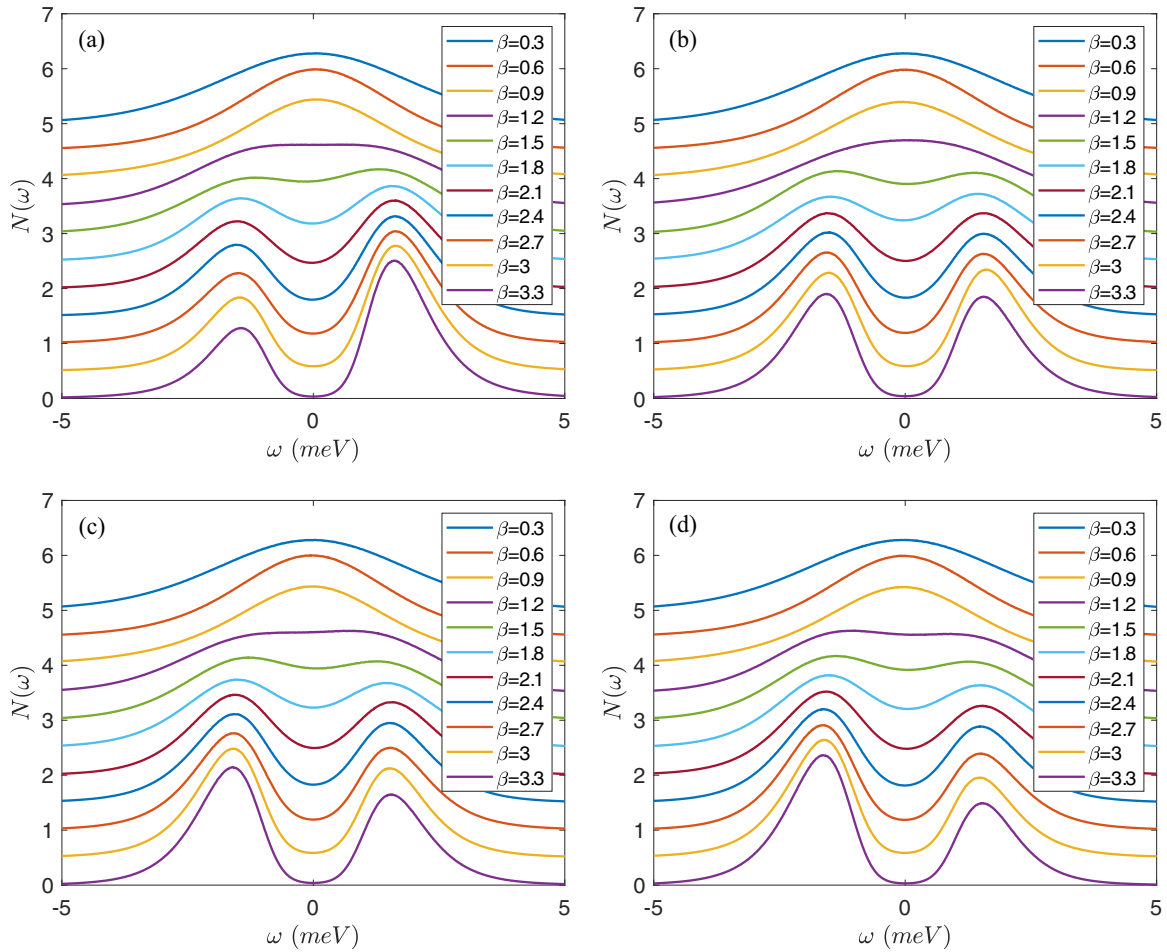
FIG. 6. DOS for $9 \times 9$ with different $\beta$ from QMC+SAC. (a)–(d) represent $\mu = -0.03, 0, 0.01, 0.02$, respectively.

explicitly breaks the SU(2) symmetry. Here, again, we use the kinetic term of a homobilayer TMD and expand the bandwidth to 0.8 meV. The same qualitative features are expected for other, more complicated setups, such as TBGs. Without the SU(2) symmetry, a BKT superconducting phase becomes allowed, and in QMC simulations we indeed observe a superconducting dome with chemical potential partially filling the flat bands, in analogy to the experiments reported in TBGs. Above the superconducting dome, the pseudogap and SCBF phases remain. Because the bandwidth is still smaller than the interaction energy scale, the temperature scales for the pseudogap and SCBF phases, which are dominated by interactions, are almost invariant for different band fillings [see Figs. 2(b) and Fig. 6], consistent with the STM experiment in TBG between different integer fillings [91]. Another observation in the TBG experiment is $d\mu/dn$ reduces towards 0 at superconducting dopings [2], which implies a large compressibility $\kappa$. This is also seen in our simulation results.

## V. DISCUSSION

We propose a model describing a 2D flat-band intervalley superconductor. The exact solution and QMC simulations reveal nontrivial phenomena, such as a doping-independent gap and large compressibility above the superconducting dome, which seems consistent with experimental studies. The supercompressible fluid phase and pseudogap phases acquire intriguing features. In transport measurements, these states are conductors, but in tunneling experiments they behave like an insulator, with a finite gap/pseudogap. However, as the system is cooled down to the superconducting phase, this gap evolves adiabatically across the superconducting transition, in direct contrast to an insulating-superconductor transition. Upon gating, the large compressibility will lead to a large response in fermion density, which is a unique feature due to moiré flat bands and distinguishes this bosonic fluid from other failed superconductors of non flat bands [92]. It is also important to point out that, despite the absence of superconductivity, the boson fluid phase may exhibit certain properties of a superconductor, e.g., Andreev reflection, because all fermions have been paired up. These Cooper pairs may also lead to other nontrivial phenomena. For example, because charge carriers now have charge 2e, an extra factor of 2 may emerge in interferometry via the Aharonov-Bohm effect. The bosonic nature of the Cooper pairs may also lead to non-Fermi liquid behavior, such as the violation of Wiedemann-Franz law, the absence or suppression of quantum oscillations and/or Friedel oscillations, and the departure of $C \propto T$ scaling in heat capacity.

## APPENDIX A: SIMULATION SETTING

In homobilayer TMDs, after two layers are rotated by a small angle $\theta$, we can see in the moiré Brillouin zone (mBZ) $+\mathbf{K}$ valley for the top and bottom layers are shifted to $\mathbf{K}_t$ and $\mathbf{K}_b$ (see, for example, Fig. 1 in Ref. [75]). A moiré continuum Hamiltonian [7,75] for the $+\mathbf{K}$ valley, which is similar to the Bistritzer-MacDonald (BM) model in Ref. [6]: $H_+(\mathbf{k}, \mathbf{r}) =$
$\left(\begin{smallmatrix} -\frac{\hbar^2(\mathbf{k}-\mathbf{K}_b)^2}{2m^*} + P_b(\mathbf{r}) & P_T(\mathbf{r}) \\ P_T^\dagger(\mathbf{r}) & -\frac{\hbar^2(\mathbf{k}-\mathbf{K}_t)^2}{2m^*} + P_t(\mathbf{r}) \end{smallmatrix}\right)$, where $b$ and $t$ refer to the bottom and top layers, $m^*$ is the effective mass, and $\mathbf{k}$ is the momentum measured from the $+\mathbf{K}$ point. The moiré potential $P_{b,t,T}$ can be parameterized as follows: $P_T(\mathbf{r}) = w(1 + e^{-i\mathbf{G}_2\cdot\mathbf{r}} + e^{-i\mathbf{G}_3\cdot\mathbf{r}})$, $P_l(\mathbf{r}) = 2w_z \sum_{j=1,3,5} \cos(\mathbf{G}_j \cdot \mathbf{r} + l\psi)$, where $l \in \{b, t\} = \{+1, -1\}$ and $\mathbf{G}_j$ are the moiré reciprocal lattice vectors with length $|\mathbf{G}_j| = \frac{4\pi}{\sqrt{3}a_M}$ and polar angle $\frac{\pi(j-1)}{3}$. Here $a_M = a_0/\theta$ is the moiré lattice constant when $\theta$ is small. These parameters were obtained from the first-principle calcula-

tions for the MoTe$_2$ homobilayer $(\hbar^2/2m^*a_0^2, w_z, w, \psi) = (495\,\text{meV}, 8\,\text{meV}, -8.5\,\text{meV}, -89.6°)$[7]. The Hamiltonian of the other valley $-K$ can be obtained by applying the time-reversal operation $H_-(\mathbf{k}, \mathbf{r}) = H_+(-\mathbf{k}, \mathbf{r})^*$.

Our form factor $\lambda_{m,n,\tau}(\mathbf{k}, \mathbf{k} + \mathbf{q} + \mathbf{G})$ is defined by $\lambda_{m,n,\tau}(\mathbf{k}, \mathbf{k} + \mathbf{q} + \mathbf{G}) = \sum_{\mathbf{G}',X} u^*_{m,\tau;\mathbf{G}',X}(\mathbf{k})u_{n,\tau;\mathbf{G}'+\mathbf{G},X}(\mathbf{k}+\mathbf{q})$, where $u^*_{m,\tau;\mathbf{G}',X}(\mathbf{k})$ is the unitary transformation matrix linking the plane-wave and band basis, while the index $X$ represents all other degrees of freedom, such as layer, sublattice, spin indices, and so on. To describe twisted TMDs, one can simply discard this subindex $X$.

For our interaction $V(\mathbf{q})$, we use a double-gate-screened Coulomb interaction

$$\frac{V(\mathbf{q})}{\Omega} \approx \frac{\theta}{N_k} \frac{4\pi}{\sqrt{3}} \frac{\tanh(\mathbf{q} \cdot \mathbf{d})}{\mathbf{q} \cdot \mathbf{a_M}}\,\text{meV}. \tag{A1}$$

Here $\theta$ is the twist angle $1.38°$, $N_k$ is the number of momentum points in mBZ, and $\mathbf{d}$ is the distance between two screened gates set as $d = 2a_M$. At this twist angle, the dispersion of the top three bands is plotted in Fig. 3.

## APPENDIX B: IMPLEMENTATION OF QMC

We follow the implementation of the momentum space quantum Monte Carlo developed by us in Ref. [59]. Starting from the Hamiltonian in the flat-band basis

$$H_I = \frac{1}{2\Omega} \sum_{\mathbf{G}} \sum_{\mathbf{q}\in mBZ} V(\mathbf{q}+\mathbf{G})\delta\rho_{\mathbf{q}+\mathbf{G}}\delta\rho_{-\mathbf{q}-\mathbf{G}},$$

$$\delta\rho_{\mathbf{q}+\mathbf{G}} = \sum_{\mathbf{k},m,n}[\lambda_{m,n,\tau}(\mathbf{k}, \mathbf{k}+\mathbf{q}+\mathbf{G})c^\dagger_{\mathbf{k},m,\tau}c_{\mathbf{k}+\mathbf{q},n,\tau}$$
$$- \lambda_{m,n,-\tau}(\mathbf{k}, \mathbf{k}+\mathbf{q}+\mathbf{G})c^\dagger_{\mathbf{k},m,-\tau}c_{\mathbf{k}+\mathbf{q},n,-\tau}]. \tag{B1}$$

According to the discrete Hubbard-Stratonovich transformation, $e^{\alpha\hat{O}^2} = \frac{1}{4}\sum_{l=\pm1,\pm2}\gamma(l)e^{\sqrt{\alpha}\eta(l)\hat{o}} + O(\alpha^4)$, where $\gamma(\pm1) = 1 + \frac{\sqrt{6}}{3}, \gamma(\pm2) = 1 - \frac{\sqrt{6}}{3}, \eta(\pm1) = \pm\sqrt{2(3-\sqrt{6})}$ and $\eta(\pm2) = \pm\sqrt{2(3+\sqrt{6})}$, we can rewrite the partition function as

$$Z = \text{Tr}\left\{\prod_t e^{-\Delta\tau H_I(t)}\right\}$$

$$= \text{Tr}\left\{\prod_t e^{-\Delta\tau \frac{1}{4\Omega}\sum_{|\mathbf{q}+\mathbf{G}|\neq0} V(\mathbf{q}+\mathbf{G})[(\delta\rho_{-\mathbf{q}-\mathbf{G}}+\delta\rho_{\mathbf{q}+\mathbf{G}})^2 - (\delta\rho_{-\mathbf{q}-\mathbf{G}}-\delta\rho_{\mathbf{q}+\mathbf{G}})^2]}\right\}$$

$$\approx \sum_{\{l_{|\mathbf{q}|,t}\}}\prod_t\left[\prod_{|\mathbf{q}+\mathbf{G}|\neq0}\frac{1}{16}\gamma(l_{|\mathbf{q}|_1,t})\gamma(l_{|\mathbf{q}|_2,t})\right]\text{Tr}\left\{\prod_t\left[\prod_{|\mathbf{q}+\mathbf{G}|\neq0}e^{i\eta(l_{|\mathbf{q}|_1,t})A_{\mathbf{q}}(\delta\rho_{-\mathbf{q}}+\delta\rho_{\mathbf{q}})}e^{\eta(l_{|\mathbf{q}|_2,t})A_{\mathbf{q}}(\delta\rho_{-\mathbf{q}}-\delta\rho_{\mathbf{q}})}\right]\right\}. \tag{B2}$$

Here $t$ is the imaginary time index with step $\Delta\tau$, and $A_{\mathbf{q}+\mathbf{G}} = \sqrt{\frac{\Delta\tau}{4}\frac{V(\mathbf{q}+\mathbf{G})}{\Omega}}$ and $\{l_{|\mathbf{q}|_1,t}, l_{|\mathbf{q}|_2,t}\}$ are the four-component auxiliary fields.

Generally, the average of any observables $\hat{O}$ can be written as

$$\langle\hat{O}\rangle = \frac{\text{Tr}(\hat{O}e^{-\beta H})}{\text{Tr}(e^{-\beta H})} = \sum_{\{l_{|\mathbf{q}|,t}\}}\frac{P(\{l_{|\mathbf{q}|,t}\})\text{Tr}[\prod_t\hat{B}_t(\{l_{|\mathbf{q}|,t}\})]\frac{\text{Tr}[\hat{O}\prod_t\hat{B}_t(\{l_{|\mathbf{q}|,t}\})]}{\text{Tr}[\prod_t\hat{B}_t(\{l_{|\mathbf{q}|,t}\})]}}{\sum_{\{l_{|\mathbf{q}|,t}\}}P(\{l_{|\mathbf{q}|,t}\})\text{Tr}[\prod_t\hat{B}_t(\{l_{|\mathbf{q}|,t}\})]}, \tag{B3}$$

$P(\{l_{|\mathbf{q}|,t}\}) = \prod_t [\prod_{|\mathbf{q}+\mathbf{G}|\neq 0} \frac{1}{16}\gamma(l_{|\mathbf{q}|_1,t})\gamma(l_{|\mathbf{q}|_2,t})]$, $\hat{B}_t(\{l_{|\mathbf{q}|,t}\}) = \prod_{|\mathbf{q}+\mathbf{G}|\neq 0} e^{i\eta(l_{|\mathbf{q}|_1,t})A_\mathbf{q}(\delta\rho_{-\mathbf{q}}+\delta\rho_\mathbf{q})} e^{\eta(l_{|\mathbf{q}|_2,t})A_\mathbf{q}(\delta\rho_{-\mathbf{q}}-\delta\rho_\mathbf{q})}$, respectively. We see $P_l = P(\{l_{|\mathbf{q}|,t}\})\text{Tr}[\prod_t \hat{B}_t(\{l_{|\mathbf{q}|,t}\})]$ as the possibility weight and $\langle\hat{O}\rangle_l = \frac{\text{Tr}[\hat{O}\prod_t \hat{B}_t(\{l_{|\mathbf{q}|,t}\})]}{\text{Tr}[\prod_t \hat{B}_t(\{l_{|\mathbf{q}|,t}\})]}$ as the sample value for configuration $\{l_{|\mathbf{q}|,t}\}$. Then the Markov chain Monte Carlo can be implemented to compute $\langle\hat{O}\rangle$.

## APPENDIX C: ABSENCE OF SIGN PROBLEM

Here, we prove there is no sign problem for our Hamiltonian. Single-particle matrices between two valleys satisfy

$$\delta\rho_{\mathbf{q}+\mathbf{G},\tau} = \sum_{\mathbf{k},m,n}[\lambda_{m,n,\tau}(\mathbf{k},\mathbf{k}+\mathbf{q}+\mathbf{G})c^\dagger_{\mathbf{k},m,\tau}c_{\mathbf{k}+\mathbf{q},n,\tau}],$$

$$\delta\rho_{\mathbf{q}+\mathbf{G},-\tau} = \sum_{\mathbf{k},m,n}[-\lambda_{m,n,-\tau}(\mathbf{k},\mathbf{k}+\mathbf{q}+\mathbf{G})c^\dagger_{\mathbf{k},m,-\tau}c_{\mathbf{k}+\mathbf{q},n,-\tau}]$$

$$= \sum_{\mathbf{k},m,n}[-\lambda^*_{m,n,\tau}(\mathbf{k},\mathbf{k}-\mathbf{q}-\mathbf{G})c^\dagger_{-\mathbf{k},m,-\tau}c_{-\mathbf{k}+\mathbf{q},n,-\tau}]$$

$$= \sum_{\mathbf{k},m,n}[-\lambda^*_{m,n,\tau}(\mathbf{k},\mathbf{k}-\mathbf{q}-\mathbf{G})\tilde{c}^\dagger_{\mathbf{k},m,-\tau}\tilde{c}_{\mathbf{k}-\mathbf{q},n,-\tau}]$$

$$= -\delta\rho^*_{-\mathbf{q}-\mathbf{G},\tau}. \tag{C1}$$

Here, $\tilde{c}_{\mathbf{k},m,-\tau} = c_{-\mathbf{k},m,-\tau}$. Then we can see that, even with flat-band kinetic terms,

$$\hat{B}_{t,\tau}(\{l_{|\mathbf{q}|,t}\}) = e^{-\Delta\tau H_{0,\tau}}\prod_{|\mathbf{q}|\neq 0}e^{i\eta(l_{|\mathbf{q}_1|,t})A_\mathbf{q}(\delta\rho_{-\mathbf{q},\tau}+\delta\rho_{\mathbf{q},\tau})}e^{\eta(l_{|\mathbf{q}_2|,t})A_\mathbf{q}(\delta\rho_{-\mathbf{q},\tau}-\delta\rho_{\mathbf{q},\tau})},$$

$$\hat{B}_{t,-\tau}(\{l_{|\mathbf{q}|,t}\}) = e^{-\Delta\tau H_{0,-\tau}}\prod_{|\mathbf{q}|\neq 0}e^{i\eta(l_{|\mathbf{q}_1|,t})A_\mathbf{q}(-\delta\rho^*_{\mathbf{q},\tau}-\delta\rho^*_{-\mathbf{q},\tau})}e^{\eta(l_{|\mathbf{q}_2|,t})A_\mathbf{q}(-\delta\rho^*_{\mathbf{q},\tau}+\delta\rho^*_{-\mathbf{q},\tau})} = \hat{B}^*_{t,\tau}(\{l_{|\mathbf{q}|,t}\}),$$

$$\text{Tr}\left[\prod_t \hat{B}_t(\{l_{|\mathbf{q}|,t}\})\right] = \text{Tr}\left[\prod_t \hat{B}_{t,\tau}(\{l_{|\mathbf{q}|,t}\})\right]\cdot\text{Tr}\left[\prod_t \hat{B}_{t,-\tau}(\{l_{|\mathbf{q}|,t}\})\right] = \left|\text{Tr}\left[\prod_t \hat{B}_{t,\tau}(\{l_{|\mathbf{q}|,t}\})\right]\right|^2. \tag{C2}$$

This is always a nonnegative number so that there is no sign problem.

## APPENDIX D: DETAILS FOR EXACT SOLUTION

First, we show the $N_d + 1$ degenerate ground states belong to one $N_d + 1$-dimensional irrep of SU(2), which can be represented by the normal Young diagram below:

$$\underbrace{\boxed{\phantom{x}}\boxed{\phantom{x}}\boxed{\phantom{x}}\cdots\cdots\boxed{\phantom{x}}\boxed{\phantom{x}}\boxed{\phantom{x}}}_{N_d} \tag{D1}$$

The dimension of irrep can be calculated by hook length formula

$$d_{[N_d]}(SU(2)) = \prod_j \frac{2+j-1}{j} = \frac{(N_d+1)!}{N_d!} = N_d + 1. \tag{D2}$$

Then, we derive the single-particle excitation of the Hamiltonian in Eq. (1). In the single-particle Hilbert subspace $H_I = \frac{1}{2\Omega}\sum_{\mathbf{G},\mathbf{q}}V(\mathbf{q}+\mathbf{G})\sum_{\mathbf{k},m,n,n',\tau}\lambda_{m,n,\tau}(\mathbf{k},\mathbf{k}+\mathbf{q}+\mathbf{G})\lambda^\dagger_{n',n,\tau}(\mathbf{k}+\mathbf{q}+\mathbf{G},\mathbf{k})c^\dagger_{\mathbf{k},m,\tau}c_{\mathbf{k},n,\tau}$, where $m,n,n'$ are flat-band labels. One can see there is no intervalley term, so it is expected that this single-particle spectrum is the same as that in the intervalley repulsion Hamiltonian, which can be seen as the red lines have the same dispersion as shown in Fig. 1. By diagonalizing $[\lambda_\tau(\mathbf{k},\mathbf{k}+\mathbf{q}+\mathbf{G})\lambda^\dagger_\tau(\mathbf{k},\mathbf{k}+\mathbf{q}+\mathbf{G})]_{m,n}$, we can obtain excited eigenstates $|\psi_{1,\mathbf{k},\tau}\rangle = c^\dagger_{\mathbf{k},\tau}|0\rangle$. Then

$(\Delta^\dagger)^n c^\dagger_{\mathbf{k},\tau}|0\rangle$ is also an excited eigenstate with the same eigenvalue $\varepsilon_{\mathbf{k},\tau}$.

We would like to normalize the ground-state and single-particle excitation states above it, such as, $|\psi_{2n}\rangle = \sqrt{\frac{(N_d-n)!}{n!N_d!}}(\Delta^\dagger)^n|0\rangle$, $|\psi_{2n+1,\mathbf{k},\tau}\rangle = \sqrt{\frac{(N_d-n-1)!}{n!(N_d-1)!}}(\Delta^\dagger)^n c^\dagger_{\mathbf{k},\tau}|0\rangle$, and $c^\dagger_{\mathbf{k},\tau}|\psi_{2n}\rangle = \sqrt{\frac{N_d-n}{N_d}}|\psi_{2n+1,\mathbf{k},\tau}\rangle$, $c_{\mathbf{k},\tau}|\psi_{2n}\rangle = \sqrt{\frac{n}{N_d}}|\psi_{2n-1,-\mathbf{k},-\tau}\rangle$, and $\Delta^\dagger|\psi_{2n}\rangle = \sqrt{(N_d-n)(n+1)}|\psi_{2n+2}\rangle$. Here $|\psi_{2n}\rangle$ and $|\psi_{2n\pm 1,\mathbf{k},\tau}\rangle$ are normalized eigenstates with $2n$ and $2n\pm 1$ electrons. According to those normalization relations, we can derive the single-particle Green's function at the zero temperature limit

$$G_{\mathbf{k},\tau}(t) = \frac{\text{Tr}(e^{-(\beta-t)H_I}c_{\mathbf{k},\tau}e^{-tH_I}c^\dagger_{\mathbf{k},\tau})}{\text{Tr}(e^{-\beta H_I})}$$

$$\stackrel{\lim_{\beta\to\infty}}{=} \frac{1}{N_d+1}\left[\sum_{n=0}^{N_d-1}e^{-t\varepsilon_{\mathbf{k},\tau}}|\langle c^\dagger_{\mathbf{k},\tau}\psi_{2n}|\psi_{2n+1,\mathbf{k},\tau}\rangle|^2\right.$$

$$\left.+ \sum_{n=1}^{N_d}e^{-(\beta-t)\varepsilon_{\mathbf{k},\tau}}|\langle\psi_{2n-1,-\mathbf{k},-\tau}|c_{\mathbf{k},\tau}\psi_{2n}\rangle|^2\right]$$

$$= \frac{1}{2}[e^{-t\varepsilon_{\mathbf{k},\tau}} + e^{-(\beta-t)\varepsilon_{\mathbf{k},\tau}}], \tag{D3}$$

note we use $t \in [0,\beta]$ instead of the usual $\tau$ to represent the imaginary time as $\tau$ has been occupied as a valley index. Besides, we can also exactly derive the imaginary time cor-

relation of Cooper pair operators at zero temperature

$$
\begin{aligned}
\langle \Delta(t) \Delta^\dagger(0) \rangle &= \frac{\text{Tr}(e^{-(\beta-t)H_I} \Delta e^{-tH_I} \Delta^\dagger)}{\text{Tr}(e^{-\beta H_I})} \\
&\overset{\lim}{\underset{\beta \to \infty}{=}} \frac{1}{N_d+1} \sum_{n=0}^{N_d-1} |\langle \Delta^\dagger \psi_{2n} | \psi_{2n+2} \rangle|^2 \\
&= \frac{N_d(N_d+2)}{6}.
\end{aligned}
\tag{D4}
$$

Since pairing correlation function $P$ is defined as $P = \frac{1}{2N_d^2} \langle \Delta\Delta^\dagger + \Delta^\dagger\Delta \rangle$, we actually achieve $P$ at zero temperature.

Next, following the proof of statement 4 in Ref. [59], we formulate in QMC framework and give a proof of relation $\langle \hat{N}_p^2 \rangle - \langle \hat{N}_p \rangle^2 = 2\langle \Delta\Delta^\dagger \rangle$ when there is no kinetic term in our Hamiltonian.

We can see $\hat{B}_{t,\tau}(\{l_{|\mathbf{q}|,t}\})$ is a unitary operator for any configuration $\{l_{|\mathbf{q}|,t}\}$. In the single-particle basis, we write the matrix form of $\prod_t \hat{B}_{t,\tau}(\{l_{|\mathbf{q}|,t}\})$ as $U = e^{M_1} e^{M_2} \cdots e^{M_n}$. According to QMC's formula, the Green's function for this configuration is defined as

$$
G_{i,j}(\tau) = \frac{\text{Tr}\left[c_{i,\tau} c_{j,\tau}^\dagger \prod_t \hat{B}_{t,\tau}(\{l_{|\mathbf{q}|,t}\})\right]}{\text{Tr}\left[\prod_t \hat{B}_{t,\tau}(\{l_{|\mathbf{q}|,t}\})\right]} = [(I+U)^{-1}]_{i,j}.
\tag{D5}
$$

By seeing $G(\tau) + G^\dagger(\tau) = (I+U)^{-1} + (I+U^{-1})^{-1} = (I+U)^{-1} + U(I+U)^{-1} = I$, we have $G_{i,j}(\tau) + G_{j,i}^*(\tau) = \delta_{i,j}$. To compute particle fluctuations, we can write $\langle \hat{N}_p^2 \rangle_l$ and $\langle \Delta\Delta^\dagger \rangle_l$ as

$$
\begin{aligned}
\langle \Delta\Delta^\dagger \rangle_l &= \left\langle \sum_{\mathbf{k}_1, m_1} c_{-\mathbf{k}_1, m_1, -\tau} c_{\mathbf{k}_1, m_1, \tau} \sum_{\mathbf{k}_2, m_2} c_{\mathbf{k}_2, m_2, \tau}^\dagger c_{-\mathbf{k}_2, m_2, -\tau}^\dagger \right\rangle_l \\
&= \sum_{\mathbf{k}_1, m_1} \sum_{\mathbf{k}_2, m_2} \langle c_{-\mathbf{k}_1, m_1, -\tau} c_{-\mathbf{k}_2, m_2, -\tau}^\dagger \rangle_l \langle c_{\mathbf{k}_1, m_1, \tau} c_{\mathbf{k}_2, m_2, \tau}^\dagger \rangle_l \\
&= \sum_{\mathbf{k}_1, m_1} \sum_{\mathbf{k}_2, m_2} |G_{\mathbf{k}_1 m_1, \mathbf{k}_2 m_2}|^2,
\end{aligned}
$$

$$
\begin{aligned}
\langle \hat{N}_p^2 \rangle_l &= \left\langle \sum_{\mathbf{k}_1, m_1, \tau_1} c_{\mathbf{k}_1, m_1, \tau_1}^\dagger c_{\mathbf{k}_1, m_1, \tau_1} \sum_{\mathbf{k}_2, m_2, \tau_2} c_{\mathbf{k}_2, m_2, \tau_2}^\dagger c_{\mathbf{k}_2, m_2, \tau_2} \right\rangle_l \\
&= \sum_{\mathbf{k}_1, m_1, \tau_1} \sum_{\mathbf{k}_2, m_2, \tau_2} \langle c_{\mathbf{k}_1, m_1, \tau_1}^\dagger c_{\mathbf{k}_1, m_1, \tau_1} \rangle_l \langle c_{\mathbf{k}_2, m_2, \tau_2}^\dagger c_{\mathbf{k}_2, m_2, \tau_2} \rangle_l + \langle c_{\mathbf{k}_1, m_1, \tau_1}^\dagger c_{\mathbf{k}_2, m_2, \tau_2} \rangle_l \langle c_{\mathbf{k}_1, m_1, \tau_1} c_{\mathbf{k}_2, m_2, \tau_2}^\dagger \rangle_l \\
&= \left( \sum_{\mathbf{k}_1, m_1} 2 - [G_{\mathbf{k}_1, m_1}(\tau) + G_{\mathbf{k}_1, m_1}^*(\tau)] \right)^2 + \sum_{\mathbf{k}_1, m_1} \sum_{\mathbf{k}_2, m_2} \sum_\tau [\delta_{\mathbf{k}_1, \mathbf{k}_2} \delta_{m_1, m_2} - G_{\mathbf{k}_2 m_2, \mathbf{k}_1 m_1}(\tau)] G_{\mathbf{k}_1 m_1, \mathbf{k}_2 m_2}(\tau) \\
&= N_d^2 + 2 \sum_{\mathbf{k}_1, m_1} \sum_{\mathbf{k}_2, m_2} |G_{\mathbf{k}_1 m_1, \mathbf{k}_2 m_2}|^2 \\
&= N_d^2 + 2\langle \Delta\Delta^\dagger \rangle_l.
\end{aligned}
\tag{D6}
$$

Since we can also easily see $\langle \hat{N}_p \rangle_l = N_d$, after averaging all configurations, we will get $\langle \hat{N}_p^2 \rangle - \langle \hat{N}_p \rangle^2 = 2\langle \Delta\Delta^\dagger \rangle$.

Finally, we would like to derive two-fermion excitations following a similar method as was used in Ref. [74]. For $\mathbf{p} \neq 0$, it is easy to check $\langle 0 | \Delta^n c_{-\mathbf{k}_2-\mathbf{p}, -\tau} c_{\mathbf{k}_2, \tau} c_{\mathbf{k}_1, \tau}^\dagger c_{-\mathbf{k}_1-\mathbf{p}, -\tau}^\dagger (\Delta^\dagger)^n | 0 \rangle = \delta_{\mathbf{k}_1, \mathbf{k}_2} A$ and $\langle 0 | \Delta^n c_{\mathbf{k}_2+\mathbf{p}, \tau}^\dagger c_{\mathbf{k}_2, \tau} c_{\mathbf{k}_1, \tau}^\dagger c_{\mathbf{k}_1+\mathbf{p}, \tau} (\Delta^\dagger)^n | 0 \rangle = \delta_{\mathbf{k}_1, \mathbf{k}_2} A$ where $A$ is a normalization constant. This means two-fermion excitations on ground states $c_{\mathbf{k}_1, \tau}^\dagger c_{-\mathbf{k}_1-\mathbf{p}, -\tau}^\dagger (\Delta^\dagger)^n | 0 \rangle$ or $c_{\mathbf{k}_1, \tau}^\dagger c_{\mathbf{k}_1+\mathbf{p}, \tau} (\Delta^\dagger)^n | 0 \rangle$ are orthogonal so that they can be seen as a well-defined basis. According to SU(2) symmetry, they should have the same excitation spectrum. By noticing $H_I$ applying on this basis forms a closed subspace

$$
\begin{aligned}
H_I c_{\mathbf{k}, \tau}^\dagger c_{\mathbf{k}+\mathbf{p}, \tau} (\Delta^\dagger)^n | 0 \rangle &= [H_I, c_{\mathbf{k}, \tau}^\dagger c_{\mathbf{k}+\mathbf{p}, \tau}](\Delta^\dagger)^n | 0 \rangle \\
&= \sum_{\mathbf{q}+\mathbf{G} \neq 0} V(\mathbf{q}+\mathbf{G}) [\lambda_\tau(\mathbf{k}, \mathbf{k}+\mathbf{q}+\mathbf{G}) \lambda_\tau(\mathbf{k}+\mathbf{q}+\mathbf{G}, \mathbf{k}) c_{\mathbf{k}, \tau}^\dagger c_{\mathbf{k}+\mathbf{p}, \tau} \\
&\quad - 2\lambda_\tau(\mathbf{k}+\mathbf{p}, \mathbf{k}+\mathbf{p}+\mathbf{q}+\mathbf{G}) \lambda_\tau(\mathbf{k}+\mathbf{q}+\mathbf{G}, \mathbf{k}) c_{\mathbf{k}+\mathbf{q}, \tau}^\dagger c_{\mathbf{k}+\mathbf{q}+\mathbf{p}, \tau} \\
&\quad + \lambda_\tau(\mathbf{k}+\mathbf{p}+\mathbf{q}+\mathbf{G}, \mathbf{k}+\mathbf{p}) \lambda_\tau(\mathbf{k}+\mathbf{p}, \mathbf{k}+\mathbf{p}+\mathbf{q}+\mathbf{G}) c_{\mathbf{k}, \tau}^\dagger c_{\mathbf{k}+\mathbf{p}, \tau}](\Delta^\dagger)^n | 0 \rangle.
\end{aligned}
\tag{D7}
$$

One can diagonalize this matrix in subspace to compute eigenexcitation states as shown in Fig. 1(a). These excitations can be $c_{\mathbf{k}_1, \tau}^\dagger c_{\mathbf{k}_1+\mathbf{p}, \tau}$ with zero charge or $c_{\mathbf{k}_1, \tau}^\dagger c_{-\mathbf{k}_1-\mathbf{p}, -\tau}^\dagger$ with charge 2e. Thus within the single-particle gap, there are continuously charged bosonic excitations.
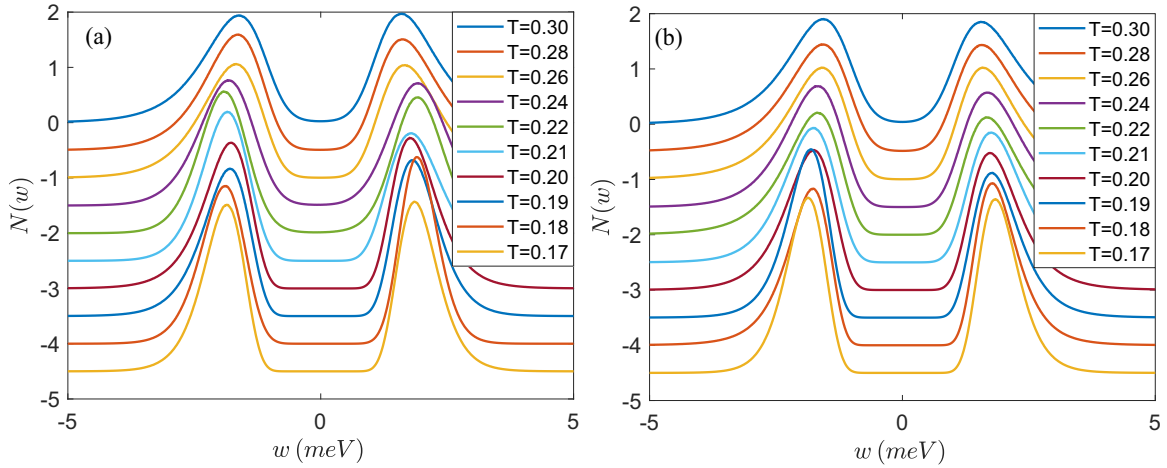
FIG. 7. DOS for $9 \times 9$ at low temperature T from QMC+SAC. (a) DOS without kinetic term. (b) DOS with kinetic term.

## APPENDIX E: ADDITIONAL FIGURES

Here, we use our exact solution results to benchmark the numerical code. As shown in Figs. 4(a) and 4(b), QMC simulations at low temperature match perfectly with the exact solution Eq. (D3) and superconductivity pairing correlation

function $P$ from QMC with increasing $\beta$ also matches the one computed from Eq. (D4). In Figs. 4(c) and 4(d), one can see the critical temperature determined by slope crossing matches well with Figs. 2(e) and 2(f) in the main text.

We show our ED results here for the $3 \times 4$ system at particle number $N = 12$ and $N = 11$ in Fig. 5. One can
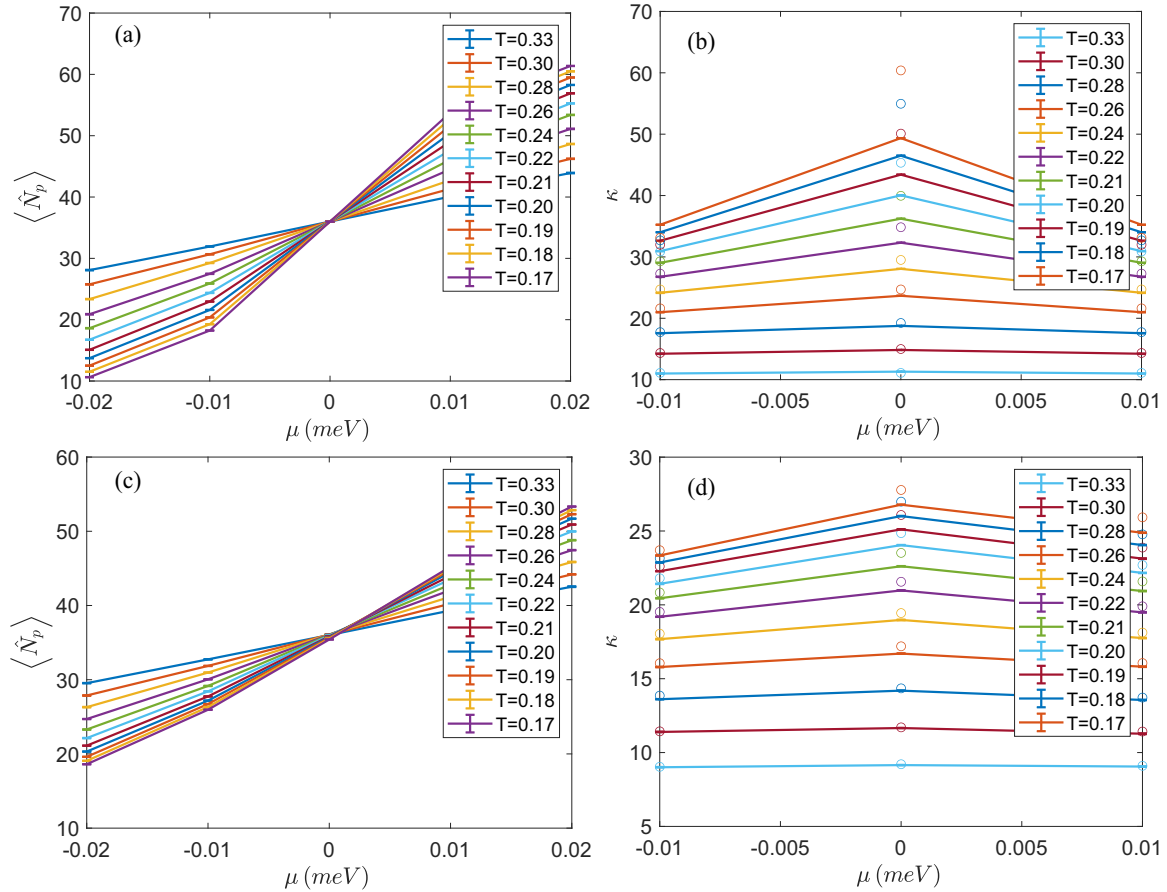


FIG. 8. Average particle number $\langle \hat{N}_p \rangle$ versus chemical potential $\mu$ for $6 \times 6$ (a) without kinetic term and (c) with kinetic term. Compressibility versus chemical potential derived from $\kappa = \frac{1}{N_d} \frac{d\langle \hat{N}_p \rangle}{d\mu}$ (colorful lines) by numerical differentiation and $\kappa = \beta \frac{\langle \hat{N}_p^2 \rangle - \langle \hat{N}_p \rangle^2}{N_d}$ (colorful circles) by QMC direct measurement (b) without kinetic term and (d) with kinetic term.

see the one-charge excitations are gapped at all momentum points and there are some excitations within the single-particle gap.

QMC + SAC DOS results with kinetic term at different chemical potential are shown in Fig. 6. One can see a small kinetic term with small chemical potential almost does not change the single-particle excitation. Also, the DOS figures below temperature $T = 0.3$ ($\beta = 3.3$) which are the low-temperature supplement of Figs. 2(c) and 2(d) are shown in Fig. 7. One can see after being fullly gapped, the position of the peak is almost unchanged around the single-particle excitation energy. It can be understood intuitively that the DOS only measures the single-particle Green's function so that the

pair excitation, which is described by two particle Green's function as shown in Fig. 4(a) within the single particle gap, cannot be observed by DOS.

The average particle number $\langle \hat{N}_p \rangle$ versus chemical potential $\mu$ is plotted with kinetic term in Fig. 8(a) and without kinetic term in Fig. 8(c) as a supplement to Figs. 2(g) and 2(h). Due to the huge compressibility at low temperature, it is hard to compute $\frac{d\langle \hat{N}_p \rangle}{d\mu}$ by numerical differentiation precisely. We use the particle fluctuation measured from QMC directly to derive the compressibility data in Figs. 2(g) and 2(h) by $\kappa = \beta \frac{\langle \hat{N}_p^2 \rangle - \langle \hat{N}_p \rangle^2}{N_d}$. The comparison of these two methods for different temperature is shown in Figs. 8(b) and 8(d).

[1] K. S. Novoselov, A. Mishchenko, A. Carvalho, and A. H. C. Neto, 2D materials and van der Waals heterostructures, Science **353**, aac9439 (2016).

[2] E. Y. Andrei and A. H. MacDonald, Graphene bilayers with a twist, Nat. Mater. **19**, 1265 (2020).

[3] C. R. Dean, A. F. Young, I. Meric, C. Lee, L. Wang, S. Sorgenfrei, K. Watanabe, T. Taniguchi, P. Kim, K. L. Shepard *et al.*, Boron nitride substrates for high-quality graphene electronics, Nat. Nanotechnol. **5**, 722 (2010).

[4] L. Wang, I. Meric, P. Huang, Q. Gao, Y. Gao, H. Tran, T. Taniguchi, K. Watanabe, L. Campos, D. Muller *et al.*, One-dimensional electrical contact to a two-dimensional material, Science **342**, 614 (2013).

[5] G. Trambly de Laissardière, D. Mayou, and L. Magaud, Localization of dirac electrons in rotated graphene bilayers, Nano Lett. **10**, 804 (2010).

[6] R. Bistritzer and A. H. MacDonald, Moiré bands in twisted double-layer graphene, Proc. Natl. Acad. Sci. USA **108**, 12233 (2011).

[7] F. Wu, T. Lovorn, E. Tutuc, I. Martin, and A. H. MacDonald, Topological Insulators in Twisted Transition Metal Dichalcogenide Homobilayers, Phys. Rev. Lett. **122**, 086402 (2019).

[8] Y. Cao, V. Fatemi, S. Fang, K. Watanabe, T. Taniguchi, E. Kaxiras, and P. Jarillo-Herrero, Unconventional superconductivity in magic-angle graphene superlattices, Nature (London) **556**, 43 (2018).

[9] Y. Cao, V. Fatemi, A. Demir, S. Fang, S. L. Tomarken, J. Y. Luo, J. D. Sanchez-Yamagishi, K. Watanabe, T. Taniguchi, E. Kaxiras *et al.*, Correlated insulator behaviour at half-filling in magic-angle graphene superlattices, Nature (London) **556**, 80 (2018).

[10] L. Wang, E.-M. Shih, A. Ghiotto, L. Xian, D. A. Rhodes, C. Tan, M. Claassen, D. M. Kennes, Y. Bai, B. Kim *et al.*, Correlated electronic phases in twisted bilayer transition metal dichalcogenides, Nat. Mater. **19**, 861 (2020).

[11] M. Yankowitz, S. Chen, H. Polshyn, Y. Zhang, K. Watanabe, T. Taniguchi, D. Graf, A. F. Young, and C. R. Dean, Tuning superconductivity in twisted bilayer graphene, Science **363**, 1059 (2019).

[12] A. L. Sharpe, E. J. Fox, A. W. Barnard, J. Finney, K. Watanabe, T. Taniguchi, M. A. Kastner, and D. Goldhaber-Gordon, Emergent ferromagnetism near three-quarters filling in twisted bilayer graphene, Science **365**, 605 (2019).

[13] X. Lu, P. Stepanov, W. Yang, M. Xie, M. A. Aamir, I. Das, C. Urgell, K. Watanabe, T. Taniguchi, G. Zhang *et al.*, Superconductors, orbital magnets and correlated states in magic-angle bilayer graphene, Nature (London) **574**, 653 (2019).

[14] M. Serlin, C. L. Tschirhart, H. Polshyn, Y. Zhang, J. Zhu, K. Watanabe, T. Taniguchi, L. Balents, and A. F. Young, Intrinsic quantized anomalous hall effect in a moire heterostructure, Science **367**, 900 (2020).

[15] U. Zondiner, A. Rozen, D. Rodan-Legrain, Y. Cao, R. Queiroz, T. Taniguchi, K. Watanabe, Y. Oreg, F. von Oppen, A. Stern, E. Berg, P. Jarillo-Herrero, and S. Ilani, Cascade of phase transitions and dirac revivals in magic-angle graphene, Nature (London) **582**, 203 (2020).

[16] Y. Saito, J. Ge, K. Watanabe, T. Taniguchi, and A. F. Young, Independent superconductors and correlated insulators in twisted bilayer graphene, Nat. Phys. **16**, 926 (2020).

[17] P. Stepanov, I. Das, X. Lu, A. Fahimniya, K. Watanabe, T. Taniguchi, F. H. Koppens, J. Lischner, L. Levitov, and D. K. Efetov, Untying the insulating and superconducting orders in magic-angle graphene, Nature (London) **583**, 375 (2020).

[18] Y. Cao, D. Chowdhury, D. Rodan-Legrain, O. Rubies-Bigorda, K. Watanabe, T. Taniguchi, T. Senthil, and P. Jarillo-Herrero, Strange Metal in Magic-Angle Graphene with near Planckian Dissipation, Phys. Rev. Lett. **124**, 076801 (2020).

[19] H. Polshyn, M. Yankowitz, S. Chen, Y. Zhang, K. Watanabe, T. Taniguchi, C. R. Dean, and A. F. Young, Large linear-in-temperature resistivity in twisted bilayer graphene, Nat. Phys. **15**, 1011 (2019).

[20] Y. Xie, B. Lian, B. Jäck, X. Liu, C.-L. Chiu, K. Watanabe, T. Taniguchi, B. A. Bernevig, and A. Yazdani, Spectroscopic signatures of many-body correlations in magic-angle twisted bilayer graphene, Nature (London) **572**, 101 (2019).

[21] Y. Jiang, X. Lai, K. Watanabe, T. Taniguchi, K. Haule, J. Mao, and E. Y. Andrei, Charge order and broken rotational symmetry in magic-angle twisted bilayer graphene, Nature (London) **573**, 91 (2019).

[22] Y. Choi, J. Kemmer, Y. Peng, A. Thomson, H. Arora, R. Polski, Y. Zhang, H. Ren, J. Alicea, G. Refael *et al.*, Electronic correlations in twisted bilayer graphene near the magic angle, Nat. Phys. **15**, 1174 (2019).

[23] D. Wong, K. P. Nuckolls, M. Oh, B. Lian, Y. Xie, S. Jeon, K. Watanabe, T. Taniguchi, B. A. Bernevig, and A. Yazdani, Cascade of electronic transitions in magic-angle twisted bilayer graphene, Nature (London) **582**, 198 (2020).

[24] X. Liu, Z. Hao, E. Khalaf, J. Y. Lee, Y. Ronen, H. Yoo, D. H. Najafabadi, K. Watanabe, T. Taniguchi, A. Vishwanath *et al.*, Tunable spin-polarized correlated states in twisted double bilayer graphene, Nature (London) **583**, 221 (2020).

[25] Y. Cao, D. Rodan-Legrain, O. Rubies-Bigorda, J. M. Park, K. Watanabe, T. Taniguchi, and P. Jarillo-Herrero, Tunable correlated states and spin-polarized phases in twisted bilayer–bilayer graphene, Nature (London) **583**, 215 (2020).

[26] C. Shen, Y. Chu, Q. Wu, N. Li, S. Wang, Y. Zhao, J. Tang, J. Liu, J. Tian, K. Watanabe *et al.*, Correlated states in twisted double bilayer graphene, Nat. Phys. **16**, 520 (2020).

[27] G. W. Burg, J. Zhu, T. Taniguchi, K. Watanabe, A. H. MacDonald, and E. Tutuc, Correlated Insulating States in Twisted Double Bilayer Graphene, Phys. Rev. Lett. **123**, 197702 (2019).

[28] G. Chen, L. Jiang, S. Wu, B. Lyu, H. Li, B. L. Chittari, K. Watanabe, T. Taniguchi, Z. Shi, J. Jung *et al.*, Evidence of a gate-tunable mott insulator in a trilayer graphene moiré superlattice, Nat. Phys. **15**, 237 (2019).

[29] G. Chen, A. L. Sharpe, P. Gallagher, I. T. Rosen, E. J. Fox, L. Jiang, B. Lyu, H. Li, K. Watanabe, T. Taniguchi *et al.*, Signatures of tunable superconductivity in a trilayer graphene moiré superlattice, Nature (London) **572**, 215 (2019).

[30] G. Chen, A. L. Sharpe, E. J. Fox, Y.-H. Zhang, S. Wang, L. Jiang, B. Lyu, H. Li, K. Watanabe, T. Taniguchi *et al.*, Tunable correlated chern insulator and ferromagnetism in a moiré superlattice, Nature (London) **579**, 56 (2020).

[31] H. Zhou, T. Xie, T. Taniguchi, K. Watanabe, and A. F. Young, Superconductivity in rhombohedral trilayer graphene, Nature (London) **598**, 434 (2021).

[32] L. An, X. Cai, D. Pei, M. Huang, Z. Wu, Z. Zhou, J. Lin, Z. Ying, Z. Ye, X. Feng, R. Gao, C. Cacho, M. Watson, Y. Chen, and N. Wang, Interaction effects and superconductivity signatures in twisted double-bilayer WSe$_2$, Nanoscale Horiz. **5**, 1309 (2020).

[33] A. Ghiotto, E.-M. Shih, G. S. S. G. Pereira, D. A. Rhodes, B. Kim, J. Zang, A. J. Millis, K. Watanabe, T. Taniguchi, J. C. Hone, L. Wang, C. R. Dean, and A. N. Pasupathy, Quantum criticality in twisted transition metal dichalcogenides, Nature (London) **597**, 345 (2021).

[34] T. Li, S. Jiang, L. Li, Y. Zhang, K. Kang, J. Zhu, K. Watanabe, T. Taniguchi, D. Chowdhury, L. Fu, J. Shan, and K. F. Mak, Continuous mott transition in semiconductor moiré superlattices, Nature (London) **597**, 350 (2021).

[35] J. M. Lu, O. Zheliuk, I. Leermakers, N. F. Q. Yuan, U. Zeitler, K. T. Law, and J. T. Ye, Evidence for two-dimensional ising superconductivity in gated MoS$_2$, Science **350**, 1353 (2015).

[36] Y. Saito, Y. Nakamura, M. S. Bahramy, Y. Kohama, J. Ye, Y. Kasahara, Y. Nakagawa, M. Onga, M. Tokunaga, T. Nojima *et al.*, Superconductivity protected by spin–valley locking in ion-gated MoS$_2$, Nat. Phys. **12**, 144 (2016).

[37] X. Xi, Z. Wang, W. Zhao, J.-H. Park, K. T. Law, H. Berger, L. Forró, J. Shan, and K. F. Mak, Ising pairing in superconducting NbSe$_2$ atomic layers, Nat. Phys. **12**, 139 (2016).

[38] Y. Ge and A. Y. Liu, Phonon-mediated superconductivity in electron-doped single-layer MoS$_2$: A first-principles prediction, Phys. Rev. B **87**, 241408(R) (2013).

[39] R. Roldán, E. Cappelluti, and F. Guinea, Interactions and superconductivity in heavily doped MoS$_2$, Phys. Rev. B **88**, 054515 (2013).

[40] N. F. Q. Yuan, K. F. Mak, and K. T. Law, Possible Topological Superconducting Phases of MoS$_2$, Phys. Rev. Lett. **113**, 097001 (2014).

[41] B. Lian, Z. Wang, and B. A. Bernevig, Twisted Bilayer Graphene: A Phonon-Driven Superconductor, Phys. Rev. Lett. **122**, 257002 (2019).

[42] J. González and T. Stauber, Kohn-Luttinger Superconductivity in Twisted Bilayer Graphene, Phys. Rev. Lett. **122**, 026801 (2019).

[43] J. Y. Lee, E. Khalaf, S. Liu, X. Liu, Z. Hao, P. Kim, and A. Vishwanath, Theory of correlated insulating behaviour and spin-triplet superconductivity in twisted double bilayer graphene, Nat. Commun. **10**, 1 (2019).

[44] Y. Wang, J. Kang, and R. M. Fernandes, Topological and nematic superconductivity mediated by ferro-SU(4) fluctuations in twisted bilayer graphene, Phys. Rev. B **103**, 024506 (2021).

[45] S. Chatterjee, M. Ippoliti, and M. P. Zaletel, Skyrmion superconductivity: DMRG evidence for a topological route to superconductivity, Phys. Rev. B **106**, 035421 (2022).

[46] E. Khalaf, S. Chatterjee, N. Bultinck, M. P. Zaletel, and A. Vishwanath, Charged skyrmions and topological origin of superconductivity in magic-angle graphene, Sci. Adv. **7**, eabf5299 (2021).

[47] H. C. Po, L. Zou, A. Vishwanath, and T. Senthil, Origin of Mott Insulating Behavior and Superconductivity in Twisted Bilayer Graphene, Phys. Rev. X **8**, 031089 (2018).

[48] C. Xu and L. Balents, Topological Superconductivity in Twisted Multilayer Graphene, Phys. Rev. Lett. **121**, 087001 (2018).

[49] B. Roy and V. Juričić, Unconventional superconductivity in nearly flat bands in twisted bilayer graphene, Phys. Rev. B **99**, 121407(R) (2019).

[50] J. F. Dodaro, S. A. Kivelson, Y. Schattner, X. Q. Sun, and C. Wang, Phases of a phenomenological model of twisted bilayer graphene, Phys. Rev. B **98**, 075154 (2018).

[51] F. Wu, A. H. MacDonald, and I. Martin, Theory of Phonon-Mediated Superconductivity in Twisted Bilayer Graphene, Phys. Rev. Lett. **121**, 257001 (2018).

[52] H. Isobe, N. F. Q. Yuan, and L. Fu, Unconventional Superconductivity and Density Waves in Twisted Bilayer Graphene, Phys. Rev. X **8**, 041041 (2018).

[53] Y.-Z. You and A. Vishwanath, Superconductivity from valley fluctuations and approximate SO(4) symmetry in a weak coupling theory of twisted bilayer graphene, npj Quantum Mater. **4**, 16 (2019).

[54] D. M. Kennes, J. Lischner, and C. Karrasch, Strong correlations and $d + id$ superconductivity in twisted bilayer graphene, Phys. Rev. B **98**, 241407(R) (2018).

[55] F. Guinea and N. R. Walet, Electrostatic effects, band distortions, and superconductivity in twisted graphene bilayers, Proc. Natl. Acad. Sci. USA **115**, 13174 (2018).

[56] M. Fidrysiak, M. Zegrodnik, and J. Spałek, Unconventional topological superconductivity and phase diagram for an effective two-orbital model as applied to twisted bilayer graphene, Phys. Rev. B **98**, 085436 (2018).

[57] S. Chatterjee, N. Bultinck, and M. P. Zaletel, Symmetry breaking and skyrmionic transport in twisted bilayer graphene, Phys. Rev. B **101**, 165141 (2020).

[58] C. Lewandowski, S. Nadj-Perge, and D. Chowdhury, Does filling-dependent band renormalization aid pairing in twisted bilayer graphene?, npj Quantum Mater. **6**, 82 (2021).

[59] X. Zhang, G. Pan, Y. Zhang, J. Kang, and Z. Y. Meng, Momentum space quantum monte carlo on twisted bilayer graphene, Chin. Phys. Lett. **38**, 077305 (2021).

[60] J. S. Hofmann, E. Khalaf, A. Vishwanath, E. Berg, and J. Y. Lee, Fermionic Monte Carlo Study of a Realistic Model of Twisted Bilayer Graphene, Phys. Rev. X **12**, 011061 (2022).

[61] G. Pan, X. Zhang, H. Li, K. Sun, and Z. Y. Meng, Dynamical properties of collective excitations in twisted bilayer graphene, Phys. Rev. B **105**, L121110 (2022).

[62] J. E. Hirsch, Discrete hubbard-stratonovich transformation for fermion lattice models, Phys. Rev. B **28**, 4059 (1983).

[63] M. Randeria, N. Trivedi, A. Moreo, and R. T. Scalettar, Pairing and Spin Gap in the Normal State of Short Coherence Length Superconductors, Phys. Rev. Lett. **69**, 2001 (1992).

[64] N. Trivedi and M. Randeria, Deviations from Fermi-Liquid Behavior Above $T_c$ in 2d Short Coherence Length Superconductors, Phys. Rev. Lett. **75**, 312 (1995).

[65] J. M. Singer, M. H. Pedersen, T. Schneider, H. Beck, and H.-G. Matuttis, From bcs-like superconductivity to condensation of local pairs: A numerical study of the attractive hubbard model, Phys. Rev. B **54**, 1286 (1996).

[66] T. Paiva, R. R. dos Santos, R. T. Scalettar, and P. J. H. Denteneer, Critical temperature for the two-dimensional attractive hubbard model, Phys. Rev. B **69**, 184501 (2004).

[67] M. Tovmasyan, S. Peotta, P. Törmä, and S. D. Huber, Effective theory and emergent SU(2) symmetry in the flat bands of attractive hubbard models, Phys. Rev. B **94**, 245149 (2016).

[68] J. S. Hofmann, E. Berg, and D. Chowdhury, Superconductivity, pseudogap, and phase separation in topological flat bands, Phys. Rev. B **102**, 201112(R) (2020).

[69] B. A. Bernevig, Z.-D. Song, N. Regnault, and B. Lian, Twisted bilayer graphene. III. Interacting Hamiltonian and exact symmetries, Phys. Rev. B **103**, 205413 (2021).

[70] N. Bultinck, E. Khalaf, S. Liu, S. Chatterjee, A. Vishwanath, and M. P. Zaletel, Ground State and Hidden Symmetry of Magic-Angle Graphene at Even Integer Filling, Phys. Rev. X **10**, 031034 (2020).

[71] O. Vafek and J. Kang, Renormalization Group Study of Hidden Symmetry in Twisted Bilayer Graphene with Coulomb Interactions, Phys. Rev. Lett. **125**, 257602 (2020).

[72] J. Kang and O. Vafek, Strong Coupling Phases of Partially Filled Twisted Bilayer Graphene Narrow Bands, Phys. Rev. Lett. **122**, 246401 (2019).

[73] B. Lian, Z.-D. Song, N. Regnault, D. K. Efetov, A. Yazdani, and B. A. Bernevig, Twisted bilayer graphene. IV. Exact insulator ground states and phase diagram, Phys. Rev. B **103**, 205414 (2021).

[74] B. A. Bernevig, B. Lian, A. Cowsik, F. Xie, N. Regnault, and Z.-D. Song, Twisted bilayer graphene. V. Exact analytic many-body excitations in coulomb hamiltonians: Charge gap, goldstone modes, and absence of cooper pairing, Phys. Rev. B **103**, 205415 (2021).

[75] H. Li, U. Kumar, K. Sun, and S.-Z. Lin, Spontaneous fractional chern insulators in transition metal dichalcogenide moiré superlattices, Phys. Rev. Res. **3**, L032070 (2021).

[76] Y. Su, H. Li, C. Zhang, K. Sun, and S.-Z. Lin, Massive dirac fermions in moiré superlattices: A route towards topological flat minibands and correlated topological insulators, Phys. Rev. Res. **4**, L032024 (2022).

[77] A. W. Sandvik, Stochastic method for analytic continuation of quantum monte carlo data, Phys. Rev. B **57**, 10287 (1998).

[78] K. Beach, Identifying the maximum entropy method as a special limit of stochastic analytic continuation, arXiv:cond-mat/0403055.

[79] A. W. Sandvik, Constrained sampling method for analytic continuation, Phys. Rev. E **94**, 063308 (2016).

[80] O. F. Syljuåsen, Using the average spectrum method to extract dynamics from quantum monte carlo simulations, Phys. Rev. B **78**, 174429 (2008).

[81] H. Shao, Y. Q. Qin, S. Capponi, S. Chesi, Z. Y. Meng, and A. W. Sandvik, Nearly Deconfined Spinon Excitations in the Square-Lattice Spin-1/2 Heisenberg Antiferromagnet, Phys. Rev. X **7**, 041072 (2017).

[82] C. Zhou, Z. Yan, H.-Q. Wu, K. Sun, O. A. Starykh, and Z. Y. Meng, Amplitude Mode in Quantum Magnets via Dimensional Crossover, Phys. Rev. Lett. **126**, 227201 (2021).

[83] G.-Y. Sun, Y.-C. Wang, C. Fang, Y. Qi, M. Cheng, and Z. Y. Meng, Dynamical Signature of Symmetry Fractionalization in Frustrated Magnets, Phys. Rev. Lett. **121**, 077201 (2018).

[84] N. Ma, G.-Y. Sun, Y.-Z. You, C. Xu, A. Vishwanath, A. W. Sandvik, and Z. Y. Meng, Dynamical signature of fractionalization at a deconfined quantum critical point, Phys. Rev. B **98**, 174421 (2018).

[85] Y.-C. Wang, M. Cheng, W. Witczak-Krempa, and Z. Y. Meng, Fractionalized conductivity and emergent self-duality near topological phase transitions, Nat. Commun. **12**, 5347 (2021).

[86] H. Li, Y. D. Liao, B.-B. Chen, X.-T. Zeng, X.-L. Sheng, Y. Qi, Z. Y. Meng, and W. Li, Kosterlitz-thouless melting of magnetic order in the triangular quantum ising material TmMgGaO$_4$, Nat. Commun. **11**, 1111 (2020).

[87] Z. Hu, Z. Ma, Y.-D. Liao, H. Li, C. Ma, Y. Cui, Y. Shangguan, Z. Huang, Y. Qi, W. Li, Z. Y. Meng, J. Wen, and W. Yu, Evidence of the Berezinskii-Kosterlitz-Thouless phase in a frustrated magnet, Nat. Commun. **11**, 5631 (2020).

[88] S. V. Isakov and R. Moessner, Interplay of quantum and thermal fluctuations in a frustrated magnet, Phys. Rev. B **68**, 104409 (2003).

[89] W. Jiang, Y. Liu, A. Klein, Y. Wang, K. Sun, A. V. Chubukov, and Z. Y. Meng, Monte carlo study of the pseudogap and superconductivity emerging from quantum magnetic fluctuations, Nat. Commun. **13**, 2655 (2022).

[90] C. Chen, T. Yuan, Y. Qi, and Z. Y. Meng, Fermi arcs and pseudogap in a lattice model of a doped orthogonal metal, Phys. Rev. B **103**, 165131 (2021).

[91] A. Kerelsky, L. J. McGilly, D. M. Kennes, L. Xian, M. Yankowitz, S. Chen, K. Watanabe, T. Taniguchi, J. Hone, C. Dean *et al.*, Maximized electron interactions at the magic angle in twisted bilayer graphene, Nature (London) **572**, 95 (2019).

[92] A. Kapitulnik, S. A. Kivelson, and B. Spivak, Colloquium: Anomalous metals: Failed superconductors, Rev. Mod. Phys. **91**, 011002 (2019).